7. Supplementary Information

Theoretical Modeling Procedure:

Theoretical modeling based upon the so-called quasi-static approximation [41-42] was applied here to describe the temperature dependence of LSRP absorption in a single Au nanoparticle much smaller than the wavelength of the incident electromagnetic radiation. The simple theory was also applied to explain the experimentally observed shift in LSPR absorption peak. An approach described in previous publications was followed using the materials parameters for Au and $SiO_2$ presented in **Table S1** [36-37, 43]. Equations S1 – S3 presented below describe the absorption cross-section ($Q_{Abs}$), the dielectric constant of Au ($\epsilon_{Au}$), and the plasmon resonance frequency ($\omega_p$ ) as a function of various material, temperature, wavelength, and particle size dependent parameters:

$$\left(Q_{Abs} = \frac{4\pi^2 a^3 \sqrt{\epsilon_m}}{2\lambda} Im\left[\frac{\epsilon_{Au}-\epsilon_m}{\epsilon_{Au}+2\epsilon_m}\right]\right) \quad \text{(S1)}$$

$$\left(\epsilon_{Au} = \epsilon_{AuFree} + \epsilon_{AuIB} = \left(1 - \frac{\omega_p^2}{\omega^2 + i\Gamma\omega}\right) + \epsilon_{AuIB}\right) \quad \text{(S2)}$$

$$\left(\omega_p = \sqrt{\frac{Ne^2}{m^*\epsilon_0}}\right) \quad \text{(S3)}$$

In Eqs. S1-S3, $a$ is the radius of the nanoparticle, $\epsilon_m$ is the dielectric constant of the matrix phase, $\epsilon_{AuFree}$ and $\epsilon_{AuIB}$ are the contributions to the dielectric constant of Au associated with free carriers and interband electronic transitions, N is the free electron density of Au, e is the charge of an electron, m* is the effective mass of free electrons, $\epsilon_0$ is the permittivity of free space, and Γ is a characteristic damping frequency for free carriers. In the context of this model, the temperature dependence of the optical absorption cross-section ($Q_{Abs}$) of a Au nanoparticle is expected to depend upon the temperature dependence of the optical constants of Au ($\epsilon_{Au}$) and the matrix phase ($\epsilon_m$). For simplicity it is assumed that the refractive index of $SiO_2$ is approximately constant over the wavelength range of interest (n=1.45 at room temperature) and the contribution

due to $\epsilon_{Au}$ associated with interband electronic transitions ($\epsilon_{AuIB}$) was assumed to be temperature independent using the models and parameters published by P. Etchegoin [44].

We have employed the theoretical approach described previously for modeling of monolithic Au films deposited on optical fibers to the nanocomposite films under investigation here [36-37, 43]. In our case the matrix phase is $SiO_2$ which exhibits a weak and roughly linear dependence of refractive index on temperature over the temperature range of interest and hence it is assumed to be described by a single thermo-optic coefficient of $dn_m/dT \sim 1.28x10^{-5}$RIU/K. In the case of Au, we make the same assumption as previous authors that the primary effect of increasing temperature is to decrease the density of free electrons due to thermal expansion and to increase the effective damping frequency of free carriers due to the increased scattering with increasing temperature. Table S1 below presents a complete table of the various parameters employed in all calculations.

| Parameter | Value | Source |
|---|---|---|
| a (nm) | 5 | Typical Au Nanoparticle Radius |
| $n_m$ | 1.45 | Typical for Dense $SiO_2$ |
| $dn_m/dT$ (Fixed) | $1.28x10^{-5}$ $K^{-1}$ | [43, 45] |
| $\omega_p$ (rad/s) | $1.314x10^{16}s^{-1}$ @ 273K, Depends on T | [43-45] |
| $\Gamma$ (rad/s) | Depends on T | [43, 45] |
| $\varepsilon_{AuIB}$ | Depends on $\lambda$ | [44] |
| $v_{Fermi}$ | $1.4x10^{15}$ nm/s | [43-45] |

**Table S1.** List of parameters used in this work and/or the reference from which the parameters were taken.

The expected reduction in free electron density, N, associated with the thermal expansion of Au translates directly into a reduction in the bulk plasmon frequency, $\omega_p$ , according to Eq. S4.

$$(\omega_p\ (T) = \omega_p\ (T_0) * \left(1 + 3\alpha(T - T_0)\right)^{-1/2}) \quad \text{(S4)}$$

The linear thermal expansion coefficient of Au can be utilized for the value of $\alpha$ for the case of Au nanoparticles in free space or loosely bound to a surface. Prior authors have made a correction to the linear thermal expansion coefficient of Au for monolithic Au films to account for an expansion in only one dimension along the film normal [43]. This particular correction is not relevant to the Au nanoparticle incorporated films and hence it was not employed as in our prior work [37].

The temperature dependence of the effective damping frequency, Γ, can be modeled by assuming a contribution associated with both electron-electron ($\Gamma_e$) and electron-phonon ($\Gamma_p$) scattering. A size dependent surface scattering term ($\Gamma_S = V_F/a$, where $V_F$ is Fermi velocity) assumed to be temperature independent has also been included to account for the finite particle size [36-37, 43].

$$(\Gamma = \Gamma_e + \Gamma_p + \Gamma_S = \Gamma_e + \Gamma_p + \frac{V_F}{a}) \quad \text{(S5)}$$

We have employed the same analytical expressions for the temperature dependence of $\Gamma_e$ and $\Gamma_p$ utilized by prior authors which are not reproduced here for brevity [36-37, 43, 46]. The simulated results of the LSPR absorption for a Au nanoparticle embedded in $SiO_2$ according to the assumptions outlined above are presented in Figure 3. A monotonic decrease in LSPR absorption peak height and an increase in peak wavelength is observed with increasing temperatures. As discussed in previous work, the former is primarily associated with the increasing resistivity of Au while the latter results from the small, positive thermo-optic coefficient of $SiO_2$ as well as the thermal expansion of Au nanoparticles [37]. The reduction in absorptance for the simulated absorption cross section for a temperature of 800$^o$C as compared to 600$^o$C is plotted in Figure 3c to illustrate the wavelength dependence of temperature sensitivity for the range of temperatures relevant for solid oxide fuel cell applications.

As discussed in prior publications [4, 37], the simple quasi-static model of Eq. S1 suggests that the origin of a gas sensing response of LSPR absorption can be attributed to changes in one or more of the following material parameters assuming that no change in Au particle size, shape, or distribution occurs: (1) the dielectric constant of the matrix phase ($\epsilon_m$), (2) the damping frequency of free carriers in the Au nanoparticles ($\Gamma$), or (3) the density of free carriers in the Au nanoparticles ($N$). The possibility of a change in $\Gamma$ as the primary origin of the gas sensing response can be ruled out as it would cause a broadening or sharpening of the LSPR absorption peak instead of a shift as experimentally observed (see Figure 2b) [4, 47]. A contribution associated with a change in refractive index of $SiO_2$ cannot be ruled out but we assume that this effect is negligible for the reasons described above. As a result, we simulate the gas sensing response in the quasi-static approximation using the simple derivative approach of Eq. S6 accounting for changes in free electron density.

$$(\Delta Q_{Abs}(\lambda) \approx \frac{\partial Q_{Abs}}{\partial N}\Big|_{\lambda} \Delta N) \quad \text{(S6)}$$

In Figure 3b, we plot the negative of the simulated $\Delta Q_{Abs}(\lambda)$ normalized to the peak value assuming a 1% increase in free electron density ($N$). The strong asymmetry about the original LSPR absorption peak position is associated with the dampening of the LSPR absorption peak by interband electronic transitions in Au.

Experimental Gas Sensing Response of Films on Planar Substrates:

Here we present gas sensing results that elucidate the wavelength dependence of the response to the reducing gases $H_2$ and CO for comparison with the theoretical modeling of Figure 3 for Au / $SiO_2$ films deposited on planar substrates. Simulated optical gas sensing tests were performed by monitoring the transmittance of Au / $SiO_2$ films in gas mixtures consisting of

flowing $N_2$, $O_2$, and $H_2$ or CO at a temperature of 850°C. For the film deposited on a planar substrate, we report sensing responses to $H_2$ only as the response to CO was observed to be relatively weak in comparison and difficult to resolve within experimental error.

The $H_2$ sensing experiment in $N_2$ or low $O_2$ content (~1%, 2% or 3% by volume) balance $N_2$ background gases are presented in **Figure S1.** These experiments consisted of 30 minute cycles of the background gas indicated and 30 minute cycles in which $H_2$ levels of 0.04, 0.2, 0.4, 1, 2, 3, and 4 volume % were introduced into the background. The 0.04% $H_2$ level was the lowest limit confidently distributed by the gas sensor testing facility. Figure S1a illustrates the film transmittance response at $\lambda$=550nm to $H_2$ up to 4% by volume in $N_2$ as well as dilute $O_2$ (~1% by volume) / balance $N_2$ backgrounds. The 0.4 volume % $H_2$ cycle for the $N_2$ background shows a higher response than the 1 volume % $H_2$ cycle but the difference is within our experimental error. As such, the data suggests a monotonic response to $H_2$ over the range experimentally investigated here for the $N_2$ and dilute $O_2$ / balance $N_2$ backgrounds. The total change in transmittance relative to the background baseline (see horizontal dashed lines) is enhanced for the dilute $O_2$ background test. For tests conducted with larger contents of $O_2$ present (e.g. 2% and 3% $O_2$ by volume), the transmittance response to $H_2$ is suppressed suggesting that $O_2$ may not be necessary for a measurable sensing response but that it can play a role in the sensing mechanism. In $N_2$ or a dilute $O_2$ (~1% by volume) background the transmittance response ($\Delta T$) illustrated in Figure S1b can be fitted to a power law in terms of the $H_2$ volume fraction (vol% $H_2$) of the following form:

$$(\Delta T = \Delta T_0 \cdot \text{vol\% } H_2^n) \qquad \text{(S7)}$$

Estimated values of $\Delta T_0$ and n obtained through the fit are $\Delta T_0$=1.27+/-0.04, n=0.12+/-0.03 and $\Delta T_0$=1.94+/-0.02, n=0.11+/-0.01 for the $N_2$ and dilute $O_2$ (~1% by volume) background,

respectively. Similar fits to the data at higher $O_2$ contents yield larger exponents of roughly 0.8-1.2 approximating a linear relationship between transmittance and vol% $H_2$ if a single point measured for the vol% $H_2$ = 4%, vol% $O_2$ = 2% gas mixture with a relatively large response is excluded but are also subject to a large absolute error (see Figure S1a). Further investigations are required to fully elucidate the mechanistic origins of the gas sensing responses observed.

A reduction in baseline transmittance at λ=550nm (see horizontal dashed lines) is observed for the $O_2$ containing background tests as compared to the $N_2$ background test suggesting that the presence of $O_2$ can also impact the LSPR absorption peak. By comparing the corresponding response at other wavelengths the change in baseline with $O_2$ can be attributed to a shift in LSPR absorption peak position opposite that which occurs during a $H_2$ exposure. These observations are consistent with a gas sensing response that is dictated by charge transfer to and from Au nanoparticles as oxidizing species such as $O_2$ would promote interactions that extract free electrons from Au while reducing species such as $H_2$ would tend to donate them effectively shifting the LSPR absorption peak in opposite directions and causing a transmission response change of opposite sign.

A $H_2$ sensing response for Au / $SiO_2$ films at 850$^o$C in a 1% $O_2$ / balance $N_2$ background and the transmittance as a function of temperature in a 20% $O_2$ / balance $N_2$ background normalized to the value at T=500$^o$C are presented in **Figure S2**. A summary of the wavelength dependence of the experimentally measured temperature response is also presented illustrating the unique wavelength dependences of the $H_2$ and temperature sensing responses. The wavelength dependences are reasonably consistent with theoretical calculations presented in Figure 3 as the peak $H_2$ response is observed near the inflection point of the LSPR absorption peak (λ~550-600nm) while the peak temperature sensitivity is observed near the LSPR

absorption peak maximum (λ~525-540nm). A zero-crossing in temperature sensitivity is also observed in the expected wavelength range. As observed for the fiber sensor, the $H_2$ response for the highest levels of $H_2$ investigated do not exhibit a zero-crossing in the wavelength range expected based upon Figure 3b. Nevertheless, unique wavelength dependences of the $H_2$ and temperature sensing responses may still potentially be exploited for simultaneous gas and temperature sensing through multiple or broadband wavelength interrogation. For the films synthesized here, $\lambda_{Temp}$~510-525nm and $\lambda_{Gas}$~565-575nm would be optimal wavelength interrogation choices to maximize the relative response to the temperature or $H_2$ content of the gas stream, respectively.

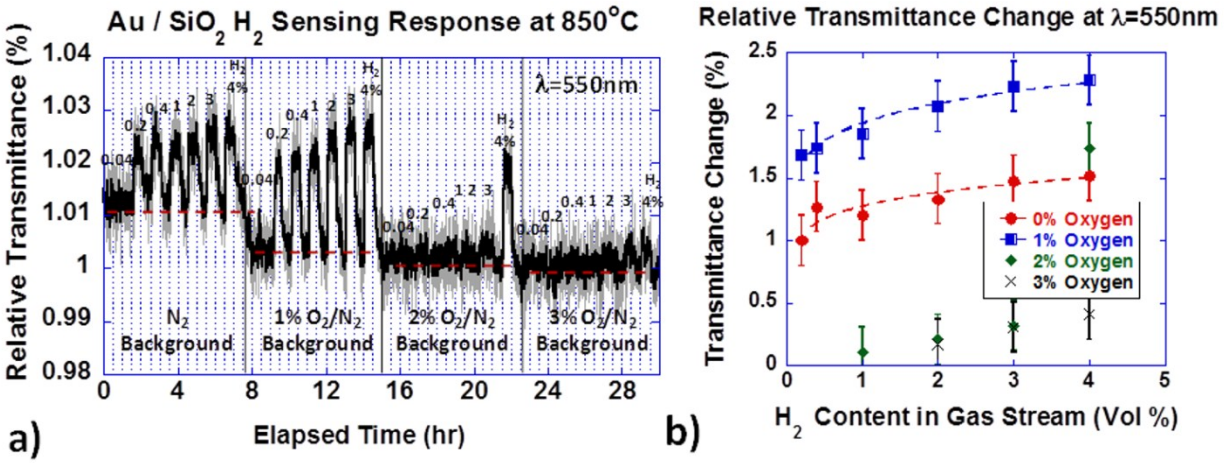


**Figure S1.** (a) Transmittance sensing response (λ=550nm) of Au / $SiO_2$ film to varying levels of $H_2$ (0.04%, 0.2%, 0.4%, 1%, 2%, 3% and 4% by volume) in a $N_2$, 1%$O_2$/$N_2$, 2%$O_2$/$N_2$, or 3%$O_2$/$N_2$ background at T=850°C with 30 minute cycles for each gas exposure. (b) Peak transmittance change relative to the baseline with varying levels of $H_2$ in different $O_2$ backgrounds at λ=550nm with the dashed lines representing the power law fits described in the text. The assumed baseline used to calculate the results of (b) for each $O_2$/$N_2$ background level is illustrated by horizontal dashed lines. The solid dark line in (a) illustrates the result of smoothing the raw data to reduce detector noise.

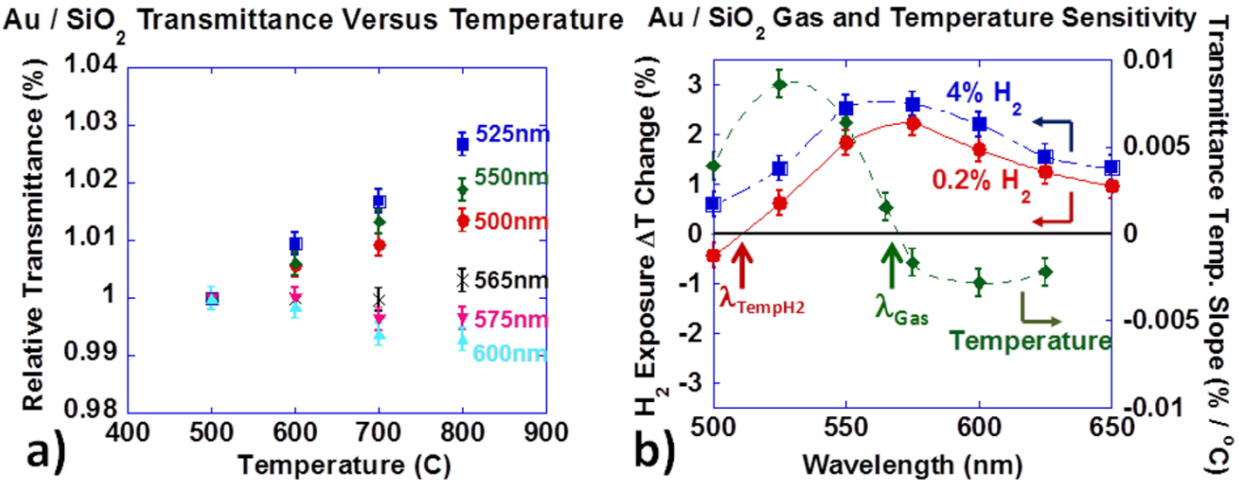


**Figure S2.** (a) Relative transmittance normalized to the value at 500°C as a function of temperature in an air atmosphere for a range of different wavelengths. (b) Summary of the wavelength dependence of the temperature and gas sensing response using the estimated slopes from a linear fit to data such as that presented in (a) over the range 600-800°C and the gas sensing results for vol% $H_2$=0.2%, 4% in a 1%$O_2$ balance $N_2$ background at T=850°C from measurements such as those presented in Figure S1.